AIAA JOURNAL
Vol. 47, No. 6, June 2009

Sound Generation and Radiation of an Open Two-Dimensional Cavity

Jonas Ask*
Volvo Car Corporation, 405 31 Göteborg, Sweden
and
Lars Davidson†
Chalmers University of Technology, 412 96 Göteborg, Sweden

DOI: 10.2514/1.32595

This work studies differences in sound generation and radiation between incompressible and compressible flowfields at the corresponding Mach number of 0.15 by evaluating the two dominant dipole terms in a temporal form of Curle's equation. The present work adds incompressible simulation results to a previously reported direct simulation of an open two-dimensional cavity oscillating in wake mode. The length-to-depth ratio of the cavity is $L/D = 4$, and the flow is considered to be laminar. The Reynolds number based on the cavity depth is $Re_D = 1500$. At these conditions, the flow is characterized by large variations in the streamwise force coefficient, showing similarities to a bluff-body wake flow, which makes the present case an attractive candidate for an incompressible approach. The root-mean-square levels of the two acoustic source terms show good agreement in the vicinity of the cavity, and the agreement in the radiated sound is almost perfect when isolating the cavity walls in the surface integration. The agreement in the radiated sound for the two flowfields is equally good when isolating the downstream wall extending from the cavity trailing edge and 10D downstream. However, when the surface integration comprises both the cavity walls and the downstream wall, a major mismatch in the directivity arises, and it is shown that this mismatch is primarily caused by an almost complete cancellation of the sources at the cavity bottom and the downstream wall in the incompressible simulations.

I. Introduction

CAVITY flows have attracted many researchers over the years, partly because of their industrial relevance for aircraft, submarines, and ground vehicles, to mention a few examples, but also because of their simple geometrical shape. In this work, the unsteady flow and noise radiation of a two-dimensional open cavity is investigated using an incompressible finite volume method. The flow oscillates in *wake mode* and shows a resemblance to a bluff-body wake flow with scales more comparable with the cavity depth than the thickness of the free shear layer downstream of the cavity leading edge. The flow is characterized by an abrupt increase in the streamwise drag force above a critical width-to-depth ratio. This makes the present case suitable for investigations of sound generation and propagation with respect to the incompressible assumption commonly used for external low-Mach-number flow predictions.

Some reports on both experimental and numerical studies exist for cavity flows oscillating in wake mode. In 1987, Gharib and Roshko [1] conducted an experimental study of the streamwise drag force as a function of the cavity length-to-depth ratio for an axisymmetric cavity, laminar upstream conditions, and a nearly incompressible flowfield. On the basis of their findings, they divided the flow regimes into *self-sustained oscillation modes* and *wake mode*. Self-sustained oscillation modes were characterized by low cavity drag due to a self-regulating positioning of the mean-shear-layer stagnation point at the cavity trailing edge. Above a critical length-to-depth ratio, they found a sudden increase in the cavity drag due to the onset of the wake-mode instability.

Compressible two-dimensional simulations of open cavities with laminar upstream conditions were studied by Colonius et al. [2]. The Mach number for their simulations was 0.6 and their findings showed a regime shift similar to that reported by Gharib and Roshko [1]. Their computational domain extended in the streamwise direction from 5D upstream of the leading edge to 7D downstream of the cavity trailing edge and 9D in the normal direction with the resolution of roughly 100 nodes per unit length (D). Buffer zones were applied over the inlet and outlet for an effective damping of fluctuations. For the wake-mode regime, they identified an intense acoustic upstream radiation, as for the shear-layer mode, but with both higher amplitude and longer wavelength.

Shieh and Morris [3] conducted two-dimensional detached eddy simulations (DES) and unsteady Reynolds-averaged Navier–Stokes (URANS) for open two-dimensional cavities at two different length-to-depth ratios. Their Mach numbers ranged from 0.4 to 0.6, and the Reynolds number for their simulation was kept constant at 200,000 based on the freestream velocity and the cavity depth. Similar to other laminar studies, a regime shift between shear-layer mode and wake mode was also identified in their simulations.

Rowley et al. [4] conducted simulations as parameter studies of Mach number, boundary-layer thickness, Reynolds number, and the length-to-depth ratio. All of their simulations were solved in two dimensions with laminar upstream boundary layers. Buffer zones were used at the inlet, outlet, and far-field boundary. For most cases, the outlet was located 10.6D downstream of the cavity leading edge, and the inlet was placed 4.3D upstream of this position. In the normal direction, the far-field boundary was located 9.2D above the cavity leading edge. The resolution in their cases was approximately 90 nodes per unit length. They found no variation in the fundamental frequency with respect to the investigated Mach numbers in their wake-mode simulations, which implied that the wake mode is not a result of acoustic feedback with respect to the shedding frequency. They also found that the shedding frequency for the wake mode was independent of the boundary-layer thickness, similar to the vortex shedding behind bluff bodies.

Presented as Paper 2992 at the 11th AIAA/CEAS Aeroacoustics Conference, Monterey, CA, 23–25 May 2005; received 4 June 2007; revision received 20 February 2009; accepted for publication 20 February 2009.

*Ph.D., Environment and Fluid Dynamics Centre, Department 91780.
†Professor, Division of Fluid Dynamics, Department of Applied Mechanics.

Larsson [5] and Larsson et al. [6] conducted two-dimensional direct simulations for an open-cavity flow oscillating in wake mode. They defined direct simulations as numerical simulations resolving both the flow scales and the acoustic scales, and this definition will also be used in this text. In all of their simulations, the Reynolds number was kept constant at 1500, based on cavity depth and the freestream velocity, and the ambient Mach number was 0.15. A laminar-boundary-layer profile was applied at the inlet combined with a buffer zone to prevent reflections. Buffer zones were also applied at the outlet and the far-field boundary. The resolution for all their cases was roughly 80 nodes per unit length (D) in the vicinity of the cavity. Their smallest resolved domain extended from $-4.3D$ upstream to $19D$ downstream of the cavity leading edge, and the largest domain extended from -4.3 to $58D$ in the streamwise direction. In the normal direction, the far-field boundary was located at 10.5 and $12.5D$ for the two different domain sizes, respectively. A comparison was then made of directly computed noise with the corresponding results computed by a temporal form of Curle's analogy. Their findings in the flowfield showed qualitative agreement with the results of both Gharib and Roshko [1] and Rowley et al. [4]. Regarding the acoustic field, they found that the region in the vicinity of the cavity trailing edge showed the highest source levels. They also found that the downstream cavity wall clearly contributed to the most-upstream-positioned observers, and the first part of the downstream wall gave a major contribution to the most-downstream-positioned observer. This finding supported the results of both Rowley et al. [4] and Colonius [7], with a clear upstream directivity caused by the cavity trailing edge due to the violent ejection of large-scale vortices from the cavity.

A further study of the same case was conducted by Ask and Davidson [8] in an attempt to find the noise generation and propagation from an incompressible flowfield. A parameter study was conducted of different time-step sizes and domain sizes and two different second-order schemes. The overall conclusion was that the levels of the two investigated dipole source terms showed good agreement in the compressible and incompressible flowfields in the vicinity of the cavity. High source levels were found at the outlet, caused by strong vortices leaving the domain. The sound directivity, however, showed a perfect match when restricting the surface integration to the cavity walls, but adding the downstream wall to the source domain caused a difference of at most 6 dB, which motivated the present work.

When computing flow-induced noise, the most straightforward method is to make a direct simulation. With this approach, it is at least theoretically possible to directly measure sound emissions at any position within the computational domain. However, this technique puts huge demands on both numerical schemes and the imposed boundary conditions, which increase with decreasing Mach number. If one instead is interested in finding the emissions at a point outside the computational domain or from an incompressible flowfield, a different strategy must be used. For flows in which walls are present, a feasible method is to use either Ffowcs Williams and Hawkings's [9] or Curle's analogy [10]. These two analogies are equivalent for steady and impermeable integration surfaces. Acoustic analogies for predicting sound radiation combined with incompressible flowfields have gained in popularity in the past years for low-Mach-number flows [11–14].

Incompressibility is a common assumption for low-Mach-number hydrodynamic-dominated flowfields and is both widely used and accepted in the computational fluid dynamics community. A consequence of this assumption is, however, a sound field identical to zero. The approach is instead to derive the acoustic analogy based on the compressible set of equations and then assume that the dominating sources of the low-Mach-number flowfield are approximately the same as the corresponding compressible sources. Although the assumption is questionable with respect to sound predictions, it has at least two benefits that make the approach attractive. First, the governing set of equations is reduced through the incompressible assumption, and second, larger time-step increments can be taken. In direct simulations the time-step size is generally limited by both the local sound wave propagation and the flow convective speed. For low-Mach-number wall-bounded flows, the limiting time-step size is the sound wave propagation.

The objectives of the present work are as follows:

1) Investigate, in comparison with previous incompressible studies of this case, the effect of convection of strong vortices over the outlet by means of applying a buffer zone at the outlet.

2) Gain a better understanding of the cause and effect of discrepancies in the radiated sound field for the incompressible treatment of the flowfield.

This paper is organized as follows. The next section describes the methodology and numerics used for the incompressible simulations. The open-cavity case is then presented, followed by the results. The final section contains conclusions.

II. Methodology

The simulations conducted in this paper are considered to be laminar (i.e., no turbulence model and laminar upstream conditions) and are all two-dimensional.

A. Buffer-Zone Evaluation

Convection of strong vortices through the computational domain can cause numerical problems when they pass the outlet. These vortices can cause local backflow, with erroneous results as a consequence. The wake-mode flow regime of the open cavity is such a case. The remedy in these occasions is traditionally to extend the domain far downstream, to increase the grid stretching or to change the outlet boundary condition.

Here, an alternative solution to this problem is investigated by adding dissipative source terms to the governing equations, which are commonly referred to as *buffer zones*, *fringe zones*, or *sponge zones* in the literature. This technique is predominantly used in direct simulations to prevent sound wave reflections generated by the outlet from polluting the sound field in the interior domain. The advantage in compressible simulations is that both the flowfield and the sound waves can be damped over the buffer zone when propagating toward the outlet. In addition, pressure perturbations caused by the outlet boundary condition can be damped when they are reflected back into the domain through the buffer zone.

In incompressible simulations, no sound waves are present, and distortions in the pressure will spread instantaneously in the whole domain and may contaminate the acoustic source terms. The purpose of buffer zones in this context is instead to dissipate the vorticity by forcing the velocities to reach a defined target level.

The test case used for the buffer-zone evaluation is a convected vortex computed in two dimensions. This test case serves mainly as a prestudy for the open-cavity case. Both geometrical dimensions and physical properties are thus chosen to be as similar as possible. The Reynolds number of $Re = 1500$ is based on the freestream velocity $U_\infty = 1.0$, the density $\rho = 1.0$, and a unit length that, for now, is denoted as D.

The computational domain is bounded by an inlet at $x_1 = -4.3D$, and the buffer-zone entrance plane or resolved domain outlet is located at $x_1 = 14.0D$. The upper boundary is placed at $x_2 = 11.0D$, and the lower boundary is positioned at $x_2 = 0$. A visual representation of the domain is shown in Fig. 1, together with the coordinate system.

The initial field consists of a disturbance superimposed to a laminar-boundary-layer profile, in which the initial disturbance is defined as

$$v_t(x_1, x_2) = -\beta r^2 \exp[-\alpha r^2] \tag{1}$$

where $r = \sqrt{(x_1 - x_{1,\text{init}})^2 + (x_2 - x_{2,\text{init}})^2}$, $\beta = 6$, $\alpha = 2$, and v_t denotes the tangential velocity. Its initial position is $x_{1,\text{init}} = 2.3D$ and $x_{2,\text{init}} = 1.7D$, and the laminar velocity profile applied at the inlet is shown in Sec. II.C. Other boundary conditions used in the test case are a no-slip condition at the lower boundary and a symmetry condition at the upper boundary. The buffer zone is the region in which the damping source terms are active. Here, they are defined as

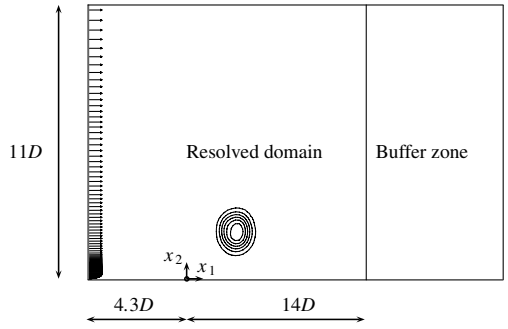

Fig. 1 Test-case description.

$$\rho\left(\frac{x_1 - x_{1,\min}}{x_{1,\max} - x_{1,\min}}\right)^n \sigma \frac{U_\infty}{D}(u_i - u_i^{\text{target}}) \tag{2}$$

where n is a shape parameter, σ is an amplification parameter, the amplification parameter $\sigma(U_\infty/D)$ is chosen in this case to be 1.0 s^{-1}, and u_i^{target} is the target state, defined here as the local time-averaged velocity vector. The source term (2) is further divided into a constant and a linear part and added to the momentum equations. The code used for the buffer-zone study is the structured finite volume method code CALC-BFC, documented by Davidson and Farhanieh [15]. The pressure is coupled to the velocity field through the SIMPLEC pressure-velocity correction algorithm, and the computational mesh is based on a single-block arrangement.

The main objective of the present study is to find a generic relation between the strength of the vortex and the buffer-zone characteristics for a mean vortex convection speed. For this purpose, the vorticity is monitored over the buffer-zone entrance plane. The vorticity in two dimensions is computed as

$$\Omega_z = \frac{\partial u_2}{\partial x_1} - \frac{\partial u_1}{\partial x_2} \tag{3}$$

Furthermore, this vorticity is averaged in the x_2 direction and monitored over time, which results in the integral value I_ω, defined as

$$I_\omega = \frac{\int_0^H (\Omega_z^{\text{rms}})\mathrm{d}x_2}{H} \tag{4}$$

where $H = 11D$. The cases investigated for the buffer-zone study are presented in Table 1, in which NC and XB are the number of cells in the x_1 direction and the length of the buffer zone, respectively. The two advection schemes used in the present study are the van Leer (VL) scheme and a second-order central-difference scheme (CDS). The shape parameter n corresponds to the exponent used in Eq. (2). The two cases, CBC (using CDS) and CBV (using VL), serve as reference solutions in which a convective outlet boundary condition is used, located at $x_1 = 14D$. The time-step size used for the test case is $\Delta t = 0.05$, which corresponds to a maximum convective Courant–Friedrichs–Lewy (CFL) number of $\text{CFL}_{\max} \approx 0.3$. The wall pressure fluctuation level is computed as

$$\text{PL} = 20\log_{10}\frac{p_w^{\text{rms}}}{p_{\text{ref}}} \tag{5}$$

where $p_{\text{ref}} = \sqrt{\rho_\infty a_\infty 10^{-12}}$ and p_w is the surface pressure.

Results of the different cases are presented in Figs. 2a–2d. Figures 2a and 2b show the rms values of the pressure along the lower wall extending from the inlet to the buffer-zone entrance plane. When the convective boundary condition is used, increased pressure fluctuations are found over those found in the buffer-zone cases (Figs. 2a and 2b). The cause of the results in these two figures can be understood by looking at the time sequence of the pressure at a point located at $x_1 = 4.2D$ and $x_2 = 0$ (Figs. 2c and 2d). When the convective boundary condition is used, both advection schemes return a pressure disturbance when the vortex leaves the domain, although its amplitude is significantly higher for the CDS scheme than for the van Leer scheme. This problem can partly be avoided by using a buffer zone, even though a small disturbance can be found in the range of $11 < t < 17$ for the CDS cases. The lowest distortion in C_p for the CDS cases is found for case B3 (Fig. 2c).

Regarding the vortex strength, all cases return similar results (Table 2) and tend to be slightly more sensitive to the advection scheme chosen as compared with the buffer-zone length and shape (Fig. 2). The most critical cases are the central-schemed cases, with a maximum vortex strength of $I_\omega \approx 0.167$, as compared with $I_\omega \approx 0.145$ for the upwind-biased cases.

For the open-cavity case, a linear relation between the vortex strength at the entrance plane of the buffer-zone and the required length of the buffer zone is assumed: that is,

$$L^{\text{OC}} = L^{\text{B3}}\frac{I_\omega^{\text{OC}}}{I_\omega^{\text{B3}}} \tag{6}$$

where superscripts B3 are the values found in case B3, and OC corresponds to the open-cavity case without a buffer zone. Case B3 is chosen because this case showed the lowest pressure distortions at location $x_1 = 4.2D$ and $x_2 = 0$ (Fig. 2c) combined with strong vorticity at the buffer-zone entrance plane. From this assumption, a minimum required length of the open-cavity buffer zone can be estimated on the basis of the findings in case B3 and the vortex strength computed for the open-cavity cases. This assumption requires that the vortex convection speed is approximately the same and that a linear assumption between different cases can be made.

B. Open-Cavity Reference Case

All incompressible open-cavity simulations conducted in this paper are compared against a direct simulation made by Larsson [5]. Because of their central part in the open-cavity investigation, some information on methodology and case setup is repeated here to give an overview of the present state of the different simulations. The reference case is entirely the work of Larsson [5] and Larsson et al. [6], and the interested reader is referred to these two publications. Larsson [5] and Larsson et al. [6] investigated the location of the domain boundaries through three different domain sizes. The computational domain for the smallest case is shown in Fig. 3. The resolved domain for the two other cases range from $-4.3D < x_1 < 46D$ to $-4.3D < x_1 < 58D$ in the streamwise direction and $-1D < x_2 < 12.5D$ to $-1D < x_1 < 14.7D$ in the lateral direction. The

Table 1 Buffer parameters and discretization schemes

Case	NC/XB	Discretization scheme	n
CBC	0	CDS	——
CBV	0	VL	——
B1	20/3.657	CDS	2
B2	20/3.657	VL	2
B3	40/7.310	CDS	2
B4	40/7.310	VL	2
B5	40/7.310	CDS	1
B6	40/7.310	VL	1

Table 2 Vortex strength results for the different cases [Eq. (4)

Case	I_ω
CBC	——
CBV	——
B1	0.167
B2	0.145
B3	0.163
B4	0.142
B5	0.167
B6	0.144

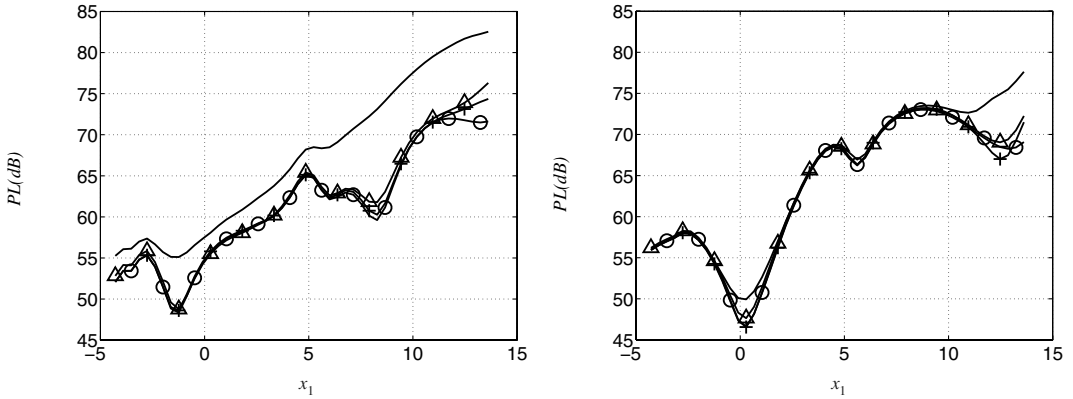

a) Wall pressure levels for the central schemed cases CBC (–), B1 (Δ), B3 (○), B5 (+)

b) Wall pressure levels for the upwind schemed cases CBV (–), B2 (Δ), B4 (○), B6 (+)

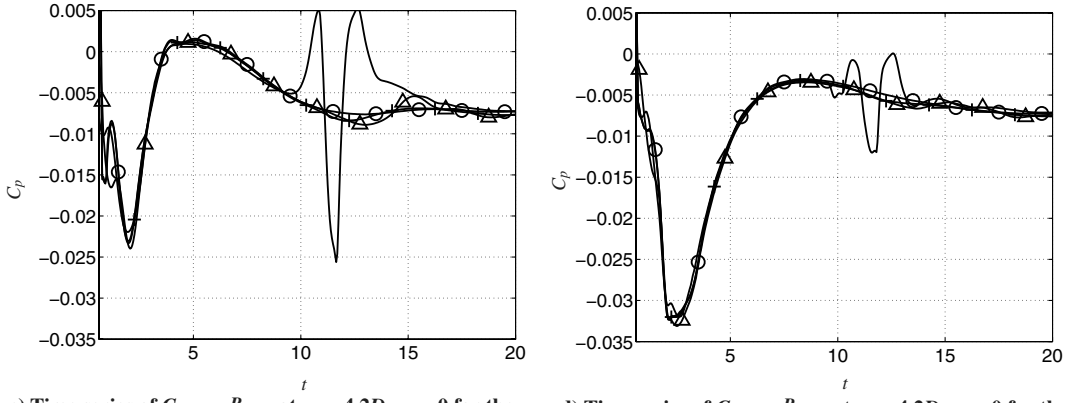

c) Time series of $Cp = \frac{P}{\frac{1}{2}\rho U^2}$, at $x_1 = 4.2D$, $x_2 = 0$ for the central schemed cases CBC (–), B1 (Δ), B3 (○), B5 (+)

d) Time series of $Cp = \frac{P}{\frac{1}{2}\rho U^2}$, at $x_1 = 4.2D$, $x_2 = 0$ for the upwind schemed cases CBV (–), B2 (Δ), B4 (○), B6 (+)

Fig. 2 Results of the buffer-zone evaluation according to Table 1.

maximum difference in overall pressure level (OAPL) between the smallest and largest domains were 0.95 dB and were found at the observer located above the cavity trailing edge. For the two cases with the largest domains, the corresponding maximum difference in OAPL was below 0.2 dB.

The advection scheme used for the inviscid fluxes was the fourth-order-accurate dispersion-relation-preserving scheme of Tam and Webb [16]. In time, an explicit four-stage fourth-order-accurate Runge–Kutta algorithm was used. The spatial resolution in the reference case was approximately 80 cells per unit length in, and in the vicinity of, the cavity. Outside the cavity, the grid was stretched less than 1%. The time-step increment was kept to $\Delta t = 0.001$. The boundary conditions in any flow simulation are of greatest importance, especially when analyzing acoustics. The boundary conditions used in the reference simulation are based on characteristic variables that are only nonreflective for orthogonal impinging waves. To prevent eventual reflections, both the inlet, outlet, and far-field region were provided with buffer zones modifying the governing equations as follows:

$$\frac{\partial Q}{\partial t} + \frac{\partial E_j}{\partial x_j} = \frac{\partial F_j}{\partial x_j} - \sigma\xi^2(Q - Q^*) \tag{7}$$

where Q is the state vector; E_j represents the inviscid fluxes; F_j represents the viscous fluxes; Q^* is the time-averaged target state; buffer parameter ξ is the nondimensional distance from the buffer-zone entrance plane to the outlet defined as x/L_b, where x is the distance from the start of the buffer zone; and L_b is the length of the buffer zone. The damping parameter is $\sigma = \sigma_0 a/L_b$, where a is the speed of sound. The values of the nondimensional amplification parameter are $\sigma_0 = 11.7$ at the inlet, $\sigma_0 = 2.07$ at the outlet, and $\sigma_0 = 11.2$ in the far-field region.

The shortest wavelength of interest was computed from the streamwise force coefficient spectrum, in which most of the energy was contained below a Strouhal number of $St \leq 4$ based on the cavity length. The minimum wavelength was then computed as follows:

$$\lambda_{\min} = \frac{a_\infty}{f_{\max}} = \frac{(U/Ma)}{(St_L \cdot U/L)} = \frac{L}{Ma \cdot St_L} \tag{8}$$

Inserting $L = 4$, $Ma = 0.15$, and the maximum Strouhal number, $St_L = 4$, gives the shortest wavelength of interest, $\lambda_{\min} \approx 7D$. In the vicinity of the cavity, the resolution is about 80 cells per cavity depth unit, resulting in an approximate resolution of 500 cells for this wavelength.

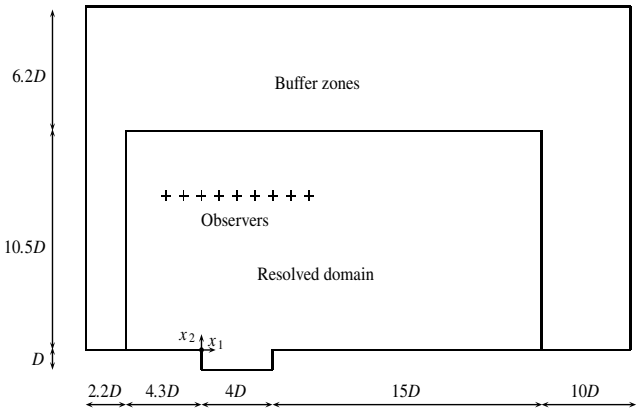

Fig. 3 Computational domain for the reference case.

This brief summary gives relevant background information for the numerical approach and case definitions for the reference case.

C. Open-Cavity Incompressible Cases

Two different schemes are used for the convective fluxes: the second-order CDS and the monotonic second-order VL [17]. Only small differences in results were found between the two discretization schemes investigated, and only the results from the CDS cases are thus presented here.

Boundary conditions used for the incompressible simulations are as follows: no-slip condition at the walls, symmetry conditions at the far-field upper boundary, and laminar-boundary-layer profiles applied at the inlet (see Fig. 4). Three incompressible cases are presented here: two cases with buffer zones at the outlet and a third case in which the buffer zone is replaced by a convective boundary condition at $x_1 = 35D$. The buffer-zone entrance plane for the two cases is located at $x_1 = 14D$.

A time step of $\Delta t U_\infty / D = 0.005$ is used for all incompressible cases and results in a maximum convective CFL number of approximately 0.5 close to the trailing edge of the cavity.

A modified version of Curle's equation is used in this work, with temporal derivatives inside the integral instead of keeping the spatial derivatives outside the integral as Curle's [10] original formulation states [Eq. (9)]:

$$p'(\mathbf{x}, t) = \frac{1}{4\pi}\frac{\partial^2}{\partial x_i \partial x_j}\int_V \frac{T_{ij}}{r}\mathrm{d}V(\mathbf{y}) - \frac{1}{4\pi}\frac{\partial}{\partial x_i}\int_S \frac{n_j}{r}(p\delta_{ij} - \tau_{ij})\mathrm{d}S(\mathbf{y}) \tag{9}$$

In Eq. (9), the acoustic pressure at an observer located at $\mathbf{x}$ is evaluated from a retarded-time projection of two integrals evaluated at the source location $\mathbf{y}$. The first integral contains the volume contribution, where

$$T_{ij} = \rho u_i u_j - \tau_{ij} + (p - a_\infty^2 \rho)\delta_{ij}$$

is commonly referred to as the Lighthill tensor.

Central to the shift from space to time in Eq. (9) is the retarded time τ, which is the time the source dynamics are evaluated as compared with the observer time t. The time lag between the source and observer depends on the speed of sound a_∞ and the distance between them, $r = |x_i - y_i|$, where x_i represents the observer location and y_i represents the source location. The source time or retarded time is defined as

$$\tau = t - \frac{r}{a_\infty} \tag{10}$$

The distance between the source and the observer, r, can also be expressed as the space lag between the source and observer according to

$$r = (t - \tau)a_\infty \tag{11}$$

Differentiation of r with respect to τ gives

$$\frac{\partial r}{\partial \tau} = -a_\infty \tag{12}$$

The differentiation of τ with respect to the observer location x_i is also needed, which gives

$$\frac{\partial \tau}{\partial x_i} = -\frac{1}{a_\infty}\frac{\partial r}{\partial x_i} \tag{13}$$

where

$$\frac{\partial r}{\partial x_i} = \frac{x_i - y_i}{|x_i - y_i|} = l_i \tag{14}$$

Differentiation of the directional vector l_i with respect to the observer location gives

$$\frac{\partial l_j}{\partial x_i} = \frac{\partial}{\partial x_i}\left(\frac{x_j - y_j}{r}\right) = \frac{\delta_{ij} - l_i l_j}{r} \tag{15}$$

The surface pressure dipole terms were given by Larsson [5] and Larsson et al. [6], identified as the two dominating terms for this open-cavity case. If the dipole terms are the main contributor to the radiated noise, Eq. (9) reduces to

$$p'(\mathbf{x}, t) \approx -\frac{1}{4\pi}\frac{\partial}{\partial x_i}\int_S \left[\frac{(p\delta_{ij} - \tau_{ij})n_j}{r}\right]\mathrm{d}S(\mathbf{y}) \tag{16}$$

Neglecting the viscous terms in Eq. (16) gives

$$p'(\mathbf{x}, t) \approx -\frac{1}{4\pi}\frac{\partial}{\partial x_i}\int_S \left[\frac{p n_i}{r}\right]\mathrm{d}S(\mathbf{y}) \tag{17}$$

The surface integral is independent of x_i, and thus the derivative can be moved inside the integral, which gives

$$p'(\mathbf{x}, t) \approx -\frac{1}{4\pi}\int_S \frac{\partial}{\partial x_i}\left[\frac{p n_i}{r}\right]\mathrm{d}S(\mathbf{y}) \tag{18}$$

Using the chain rule

$$\frac{\partial}{\partial x_i} = \frac{\partial \tau}{\partial x_i}\frac{\partial}{\partial \tau}$$

in Eq. (18) and carrying out the differentiation with respect to time gives

$$p'(\mathbf{x}, t) \approx -\frac{1}{4\pi}\int_S \frac{\partial \tau}{\partial x_i}\left[\left(\left(\frac{\partial p}{\partial \tau}r - p\frac{\partial r}{\partial \tau}\right)\Big/ r^2\right)n_i\right]\mathrm{d}S(\mathbf{y}) \tag{19}$$

Replacing $\partial p/\partial \tau$ with $\dot{p}$ to simplify the notation and replacing the derivatives according to Eqs. (12–14) gives the final expression:

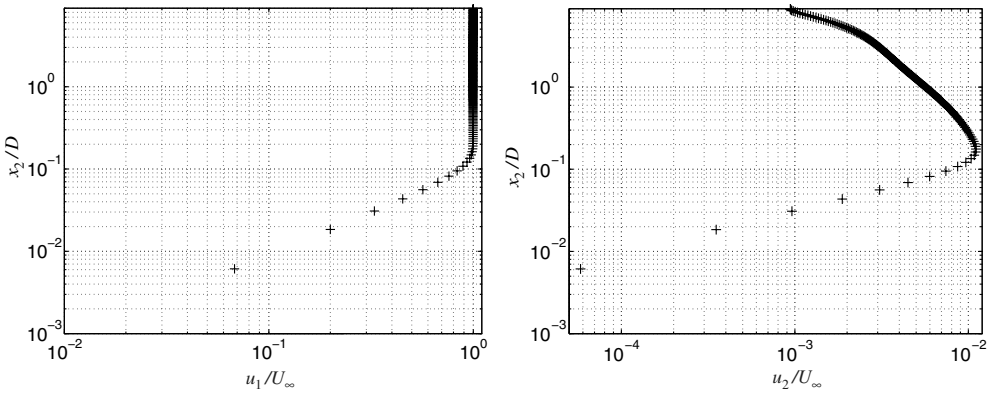

a) Inlet u_1-profile **b) Inlet u_2-profile**

Fig. 4 Boundary-layer profiles at the inlet.

$$p'(\mathbf{x},t) \approx \frac{1}{4\pi}\int_S l_i\left[\frac{p}{r^2}n_i\right]\mathrm{d}S(\mathbf{y}) + \frac{1}{4\pi a_\infty}\int_S l_i\left[\frac{\dot{p}}{r}n_i\right]\mathrm{d}S(\mathbf{y}) \quad (20)$$

The dot above p denotes the time derivative, and l_j is the unit vector pointing from the source to the observer.

Equation (20) is valid for three dimensions, whereas the flowfield is computed in two dimensions. Thus, the flowfield is expanded in the spanwise direction. A sensitivity study of this expansion was conducted in [5,6], and the present work uses a spanwise expansion identical to that used in the compressible reference simulations.

In the present work, source terms 1 and 2 in Eq. (20) refer to the fluctuating wall pressure and its time derivative, respectively, and are the only terms investigated here.

III. Description of the Open-Cavity Case

The present case is an upstream laminar flow past an open-cavity with a length-to-depth ratio of $L/D = 4$ and a Reynolds number of $Re_D = 1500$ based on the cavity depth. The length L is the streamwise extension between the cavity leading and trailing edges, and the depth D is the normal extension from the cavity bottom to the origin of the coordinate system (see Fig. 5). The following definitions are used. The inlet wall extends from the inlet to the cavity leading edge. The cavity itself consists of the cavity upstream wall, the cavity bottom, and the cavity downstream wall. The wall extending from the cavity trailing edge to the buffer-zone entrance is defined as the outlet wall.

The resolution for the incompressible cases is kept constant in the cavity, with roughly 80 cells per unit length in each direction. The domain is resolved by 900 nodes in the streamwise direction and 250 nodes in the flow normal direction. The two buffer-zone cases are case C1, with the shortest buffer-zone length, $5D$, and case C3, with a buffer-zone length of $11.4D$. The $5D$ buffer-zone length in case C1 is the shortest length to fulfill [Eq. (6)]. For case C5, the buffer zone is replaced by a convective boundary condition (see Table 3). In Table 3, "end of resolved domain" and "end of domain" refer to the x_1 direction measured from the origin of the coordinate system. The computational domain used for the incompressible cases is also presented in Fig. 5.

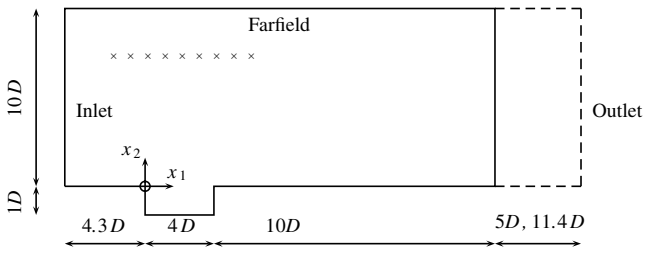

Fig. 5 Geometrical dimensions for the open-cavity case.

Table 3 Case description

Case ID	Outlet treatment	End of resolved domain	End of domain
Ref	Buffer zone	$19D$	$29D$
C1	Buffer zone	$14D$	$19D$
C3	Buffer zone	$14D$	$25.4D$
C5	Convective bc	$35D$	$35D$

Table 4 Observer locations

Observer	x_1	x_2
1	$-2D$	$7.18D$
2	$-1D$	$7.18D$
3	$0D$	$7.18D$
4	$1D$	$7.18D$
5	$2D$	$7.18D$
6	$3D$	$7.18D$
7	$4D$	$7.18D$
8	$5D$	$7.18D$
9	$6D$	$7.18D$

The acoustic part of this work contains comparisons of the sound directivity at nine equally distributed observers above the cavity. The positions of these observers are given in Table 4 and in Fig. 5.

The simulation time contains at least five full flow cycles after the decay of the initial transients. Statistic convergence is determined here based on the time sequence of the cavity streamwise force coefficient. Because the flow is periodic, acoustic source information was only extracted during the last flow cycle, as was done in the reference simulation.

IV. Validation of the Flowfield

Cavity flows in wake mode are characterized by violent ejections of vortices from the cavity, with length scales that are comparable with the cavity dimensions rather than with the thickness of the boundary layer. This oscillatory flowfield is associated with both high mean drag and large variations in the streamwise force within each period, as compared with the self-sustained oscillation modes. Figure 6 shows the time sequence of the cavity drag for case C1 and the reference case. The streamwise cavity drag is computed as

$$C_D = F_D/(\tfrac{1}{2}\rho_\infty U_\infty^2 D) \quad (21)$$

where F_D (in newtons) is the force contribution from the three cavity walls and consists of the wall normal pressure at the cavity upstream and downstream walls and the friction contribution at the cavity bottom.

As can be seen in Figs. 6a and 6b, the ejection of large vortex structures generates large variations in the cavity drag, with a clear

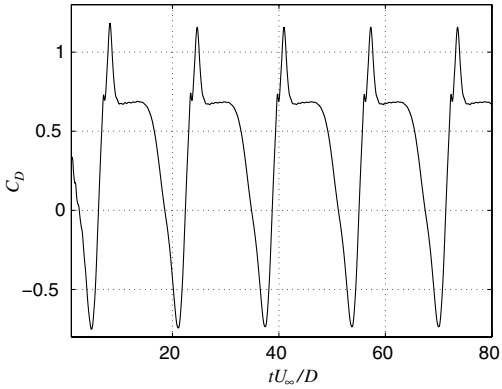

a) C_D history of case, C_1

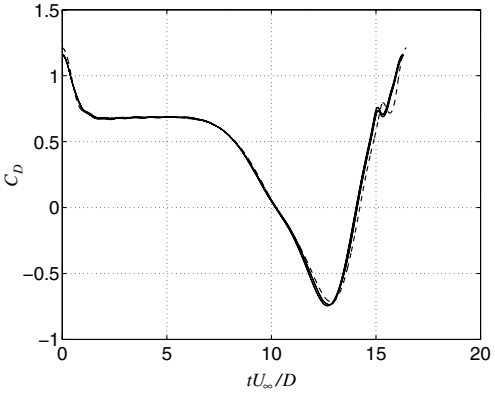

b) C_D over the last period for cases, (– –) Ref, (–) C1, at fully developed condition

Fig. 6 C_D history versus time units.

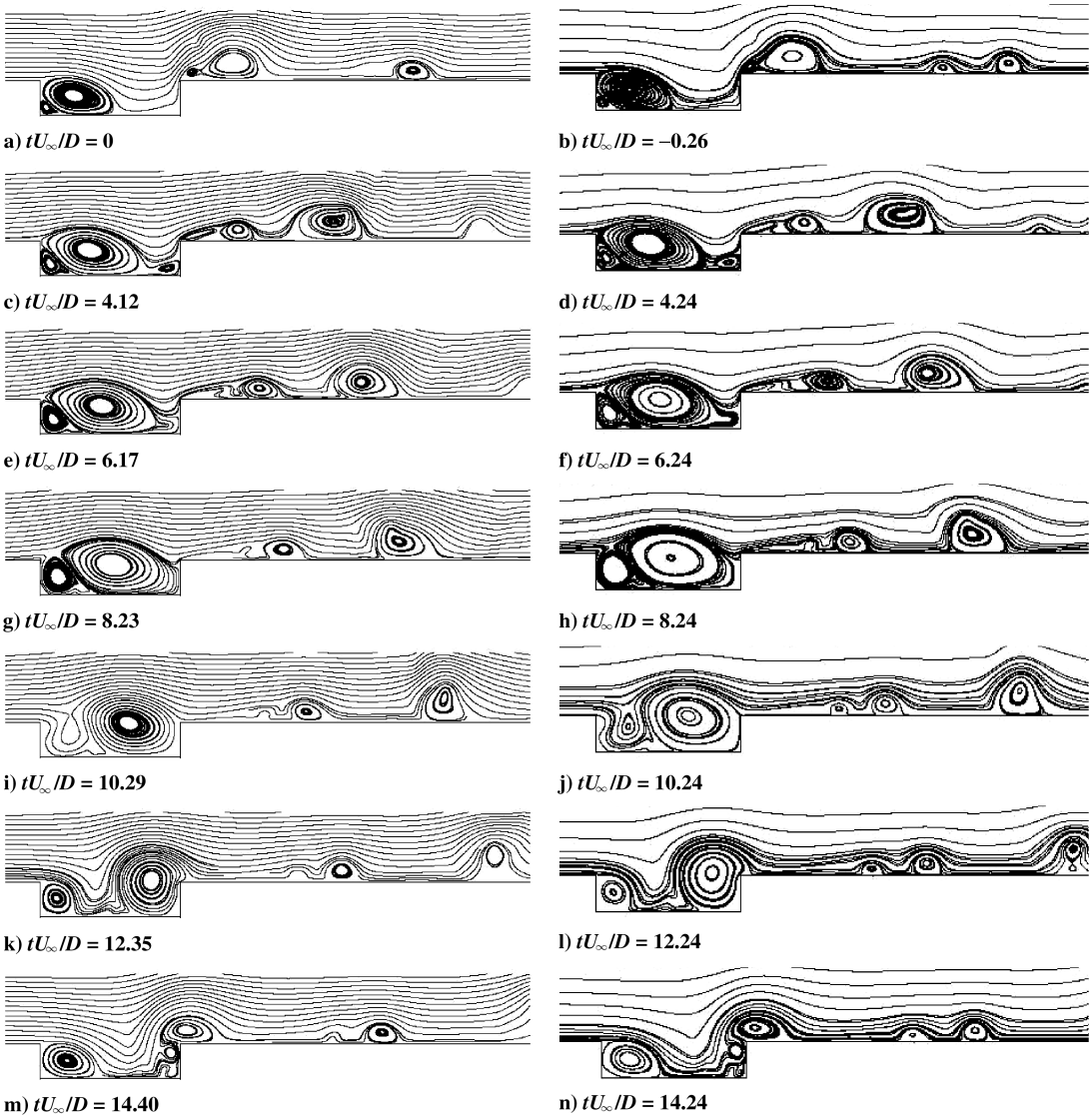

Fig. 7 Streamlines: compressible (left) and incompressible (right).

periodic content, and agrees well with the reference case (see Fig. 6b). The time average of the drag varies between $0.377 < \bar{C}_D < 0.379$ for the incompressible cases, and the reported values for the reference case are $\bar{C}_D = 0.384$ for the shorter domain and $\bar{C}_D = 0.377$ for the extended domain. The cause of the rapid changes in the cavity drag can be understood by looking at snapshots of the flow in Fig. 7, in which each snapshot pair is synchronized with the cavity drag cycle in Fig. 6b. The upper left and lower right corners in every figure are located at $(x_1, x_2) = (-1D, 2D)$ and $(x_1, x_2) = (14D, -1D)$, respectively.

A visual comparison of streamline snapshots can give indications of differences in the present flow structures. These snapshots already existed for the reference case, and the incompressible snapshots were extracted at times as closely as possible. Before further discussing the results and the coupling between the flowfield and the cavity drag, common attributes in vortex structures and the flow pattern of the present case will briefly be described.

Several major vortices are generated during one cycle of period. The first and most dominant is the primary clockwise-rotating vortex evolving from the recirculation bubble at the upstream cavity wall (Figs. 7k and 7l). This primary clockwise vortex dictates the fundamental frequency of the cavity flow and initially grows rapidly within the cavity (Figs. 7m and 7n to Figs. 7g and 7h through Figs. 7a and 7b). The growth of this vortex ends when the connection to the cavity leading edge is lost and the freestream is partly directed to the cavity bottom upstream this vortex (Figs. 7i and 7j). This initiates an ejection phase in which the vortex decreases in size and starts a motion normal to the cavity bottom (Figs. 7k and 7l). As the primary vortex ejects from the cavity, a smaller but much stronger counterclockwise-rotating vortex is generated at $(x_1, x_2) = (3.9D, -0.3D)$ (see Figs. 7m and 7n). This vortex splits the primary clockwise-rotating vortex into one major vortex located at $(x_1, x_2) = (4.2D, 0.5D)$ and one minor vortex located at $(x_1, x_2) = (3.5D, -0.7D)$ (Figs. 7m and 7n). The counterclockwise-rotating vortex decays rapidly outside the cavity and can only be seen in Figs. 7a and 7b as a deflection of the streamlines at $x_1, x_2 = 4.5, 1.2D$. When the position of the major vortex is slightly downstream of the cavity trailing edge, one full cycle is completed (Figs. 7m and 7n). As the primary vortex has left the cavity, high-speed fluid is redirected into the cavity, causing a jetlike flow at the cavity trailing edge. One of these vortices merges with the major cavity vortex and contributes to its asymmetrical shape (Figs. 7c and 7d) at $(x_1, x_2) = (9D, 1.0D)$.

If we look at the cavity drag (Fig. 6b), we see that the maximum peak occurs as the primary vortex leaves the cavity, exposing the downstream cavity face to the freestream (Figs. 7a and 7b). The cavity drag is nearly constant at $1 < tU_\infty/D < 6$ but drops rapidly when the primary cavity vortex attaches to the downstream cavity wall, redirecting the rear stagnation point from the lower part of the cavity downstream wall to the cavity trailing edge. As the vortex starts to eject from the cavity, the lowest drag value is found to be caused by a low-pressure zone at the cavity downstream face (Figs. 7k and 7l).

At first glance, the snapshots in Figs. 7 look identical for both flowfields. Some minor differences can, however, be detected in Figs. 7a and 7b in the individual position and strength of the vortex pair at $10D < x_1 < 12D$. The different strength is most probably a postprocessing issue for the reference case, because the streamlines are clearly deflected. However, both their individual distance and their global position differ slightly.

The periodicity of the flow can be described by the fundamental or Strouhal frequency, defined as

$$St_L = fL/U_\infty \tag{22}$$

where St_L is the Strouhal number and f is the fundamental frequency. All incompressible cases give a Strouhal number of $St_L = 0.245$ and the reported compressible results vary between $0.243 < St_L < 0.245$.

The conclusion drawn from the flowfield part is that the cavity drag and the periodicity are the same for the two flowfields. Regarding the flow pattern in the cavity, the streamline snapshots also indicate almost identical results. There are, however, some visual differences starting at approximately $x_1 = 8D$, where the intermediate vortex seems to be more rapidly convected toward the outlet for the incompressible case than for the reference case.

V. Acoustic Results

Figure 8 shows the rms levels of the two wall source terms [Eq. (20)] as a function of the wall perimeter s/D (s/D is, for example, 0 and 6 at the leading and trailing edges, respectively). Although the difference is not clearly seen in the two figures, all the incompressible cases show an almost singular behavior at the cavity trailing edge, whereas the reference case is smoothly damped. The source levels in this region are thus highly dependent on the resolution and are not believed to be better predicted with higher resolution. Except for this fact, the agreement between the different cases is perfect upstream $s/D = 11$ for source term 1 (Fig. 8a). In the region $s/D = 11$ to 13, all incompressible cases somewhat underestimate somewhat the reference rms level. This is the region in which streamline snapshots (Figs. 7a and 7b) showed visual differences in the flowfield. However, it is believed that this mismatch in results is neither sufficiently large nor in such proximity to the observers to be of major importance. The second source term (Fig. 8b) shows, in comparison, discrepancies both close to the inlet and downstream $s/D = 8$. All incompressible cases had identical boundary conditions at the inlet, and a buffer zone was applied for the reference case. This difference in treatment had no apparent effect for source term 1, but a mismatch arose for source term 2. For the latter source term, all incompressible cases show almost identical results from the inlet to the cavity leading edge. The results look slightly different at the outlet. In this region, the incompressible cases are not as aligned as at the inlet, but the results for this source term instead show individual spreading. In comparison with the inlet, all cases have different treatments of the downstream part of the flow. One possible conclusion that can be drawn from these two regions is that the buffer zone has a primary impact in the flow time scales, which can have a significant effect in the radiated sound. However, the alternative of replacing the buffer zone with a convective boundary condition gives no improvement in the source rms level, as can be seen from the figure.

The findings show that both source terms have their maximum close to the cavity trailing edge. The region with the second-highest value differs slightly for the two source terms. The fluctuating pressure term shows the second-highest peak at the cavity bottom at $s/D \approx 4$ whereas the corresponding peak for the pressure temporal derivative term occurs at $s/D \approx 11$ (see Figs. 8a and 8b, respectively). Common for all incompressible cases is an overprediction of the pressure temporal derivative term in the region $8D < s < 12D$, downstream of the cavity trailing edge. If we go back and look at Figs. 7i–7n and then Figs. 7a and 7b, which is the next snapshot in the periodic sequence, a small trailing vortex can be identified in this region. This vortex is present in both flowfields but is stronger in the incompressible flowfield and vanishes downstream in the compressible case (Fig. 7a). The vortex originates from the jetlike flow at the cavity trailing edge, which is overpredicted in the incompressible cases.

No comparison of the two source terms can be made by simply looking at the different levels. The only way to compare them quantitatively is as source terms to Curle's analogy or some other method to make evaluations at different observer positions. At these locations, the pressure level (PL) is computed as

$$\mathrm{PL} = 20\log_{10}\left(\frac{\phi_{l,\mathrm{rms}}}{p_{\mathrm{ref}}}\right) \tag{23}$$

where $p_{\mathrm{ref}} = \sqrt{\rho_\infty a_\infty 10^{-12}}$ and $\phi_{l,\mathrm{rms}}$ is the source rms level. The source index l represents the fluctuating wall pressure ($l = 1$) and the pressure temporal derivative ($l = 2$).

Figure 9 shows a comparison of the contribution from the two individual source terms using Eq. (20). The directivity of the incompressible cases and the reference case looks similar for source term 1, but the levels for all the incompressible cases are generally overpredicted. At the observer positioned farthest upstream, the incompressible cases show an approximate offset of 2 dB compared with the reference case. This offset increases further downstream, as does the individual spreading between the incompressible results. At the observer positioned farthest downstream, both the spreading and the offset between the incompressible and compressible results are again reduced. As seen in Fig. 8a, the rms level was almost identical in the two flowfields. Similar to source term 1, the results for source term 2 also show the highest agreement at the observer positioned farthest upstream and the overprediction also becomes more pronounced further downstream. At the observer positioned farthest downstream, the results converge as for source term 1, but only in the buffer-zone cases. The results when both source terms are included in the surface integration are shown in Fig. 10.

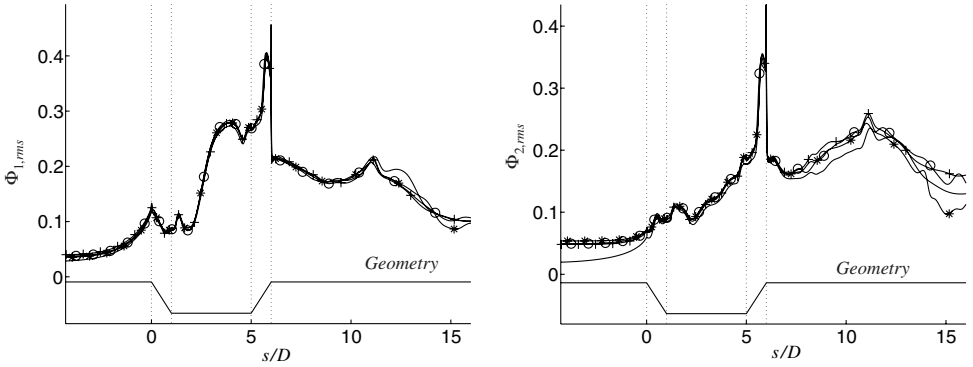

a) Source term 1 **b) Source term 2**

Fig. 8 Root mean square of the two source terms: reference (−), C1 (+), C3 (★), and C5 (○).

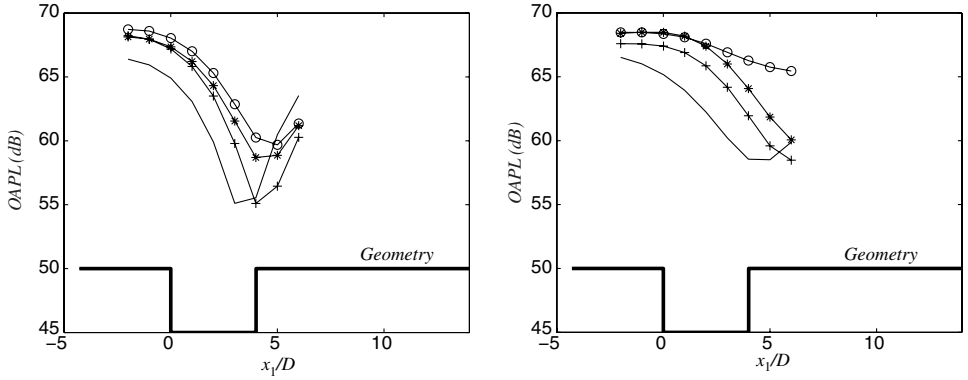

a) Source term 1 **b) Source term 2**

Fig. 9 OAPL at the observers for the two source terms: reference (−), C1 (+), C3 (★), and C5 (○).

Comparison of the incompressible cases shows as much as a 6 dB discrepancy for the observer located farthest downstream, whereas the source rms levels were almost identical for both source terms. When comparing the incompressible cases with the reference case, a maximum discrepancy of approximately 7 dB is found for observer 7 located at $(x_1, x_2) = (4D, 7.18D)$. This large difference is present only for the case without a buffer zone, indicating problems associated with the outlet treatment. Compared with the reference case, a 2–3 dB offset is present for all incompressible cases for the observer located farthest upstream. The downstream directivity, on the other hand, shows a strong sensitivity in the streamwise location for the reference case, which is replaced by a much smoother curve for all incompressible cases. This sensitivity in the streamwise location is less pronounced for case C5, the case without a buffer zone.

To gain a better understanding of the cause and effect of the present results, the solid walls are split into segments to check their contribution individually. In Fig. 8, discrepancies in the two source terms were found at the outlet wall, but are argued to be of less importance because of both the level and distance to the closest observer. Successively adding portions of the outlet wall to the surface integration (see Fig. 11) illustrates the importance of the mismatch in source levels with respect to the observers and shows the convergence of the pressure levels with respect to the proximity of the outlet boundary. Figure 11 shows that the mismatch in the rms levels for the downstream source region has little importance for the directivity at the nine observers. The results indicate that the last $6D$ part of the outlet wall has no significant influence on the pressure level at the observers.

The next part of the analysis is the cavity itself. The agreement in source levels for these walls is even better than for the outlet wall (see Fig. 9). When integrating over these three surfaces, the directivity between the two flowfields matches almost perfectly (see Fig. 12a).

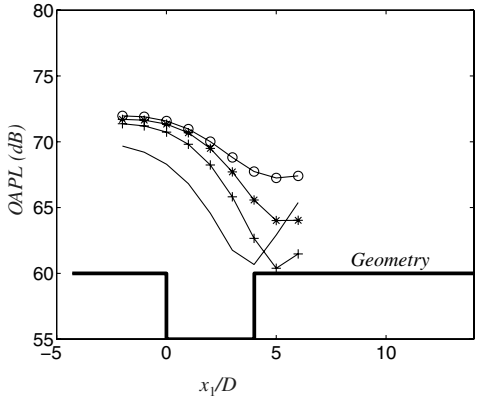

Fig. 10 OAPL for the nine observers, all solid walls: reference (−), C1 (+), C3 (★), and C5 (○).

The directivity from this part differs from the outlet wall in a more pronounced peak at the middle observer. The curves are also slightly asymmetric due to the higher source levels at the cavity downstream wall, which amplify the pressure levels for the observers positioned farthest upstream (see Fig. 12a). Expanding the integration surface by first adding the closest $2D$ upstream part of the inlet wall and then the whole inlet wall reveals one source of error. The offset in directivity arises between the two flowfields, most probably due to the inlet boundary condition. This offset increases when approaching the inlet and can also be isolated by simply integrating over the inlet wall (see Fig. 12d).

Thus far, the cavity walls, the inlet wall, and the downstream wall have been investigated individually. The next step is to successively combine these parts in the integration. Figure 13a includes the outlet wall and the upstream and downstream walls of the cavity in the integration. The results indicate that the cavity trailing edge is not the cause of the discrepancies seen in Fig. 10. Compared with Fig. 11c, cancellation of the sources at the two cavity walls and the outlet wall reduces the OAPL for the observers located farthest upstream by approximately 5 dB. Adding the inlet wall to the former parts gives the results shown in Fig. 13b. The only wall section not included in the surface integration is now the cavity bottom wall. The two incompressible cases, C3 and C5, now show similar results, with a maximum discrepancy of less than 1 dB for the six observers positioned farthest downstream. For the third incompressible case, C1, the results now look slightly different. Contrary to the other two incompressible cases, a maximum discrepancy of approximately 1.5 dB occurs at the observer positioned farthest upstream, which reduces downstream and meets the other two incompressible cases at the observer positioned farthest downstream. However, the overall result thus far is indeed surprising. The incompressible cases show an OAPL that agrees fairly well with the reference case and, in comparison with Fig. 10, the last wall part that makes this difference is the cavity bottom wall. Finally, adding the cavity bottom wall to the cavity walls and the outlet wall gives the result shown in Fig. 13c. Another way to illustrate the effect of the cavity bottom wall compared with the other walls is to compare the results in Fig. 13c with those in Fig. 13a. The results indicate that the phase of the sources at the cavity bottom wall compared with the other walls differs between the compressible and the incompressible flowfields or that the differences found are caused by an almost complete cancellation of different sources. This means that even if the amplitude of the most dominant structures are captured correctly, which is what the rms level represents, large deviations in the total acoustic pressure can still occur if small perturbations occur at a point in time when the main sources cancel each other. One way to analyze this situation is to instead study the acoustic signature from the different surface segments directly. Of the nine observers, the largest discrepancy was found for observer 7, located directly above the trailing cavity edge. Therefore, this observer was used in the following analysis.

The effect on the acoustic signals of using the buffer zone as compared with the convective outlet boundary condition is shown in

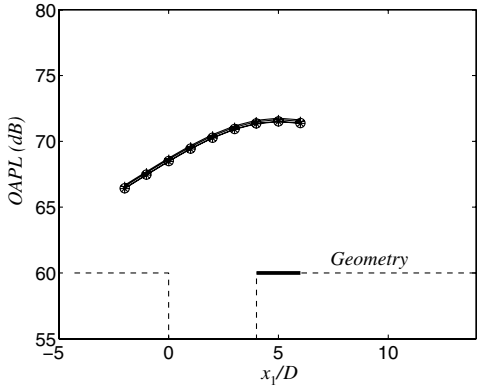

a) Integration from the trailing edge and 2*D* downstream

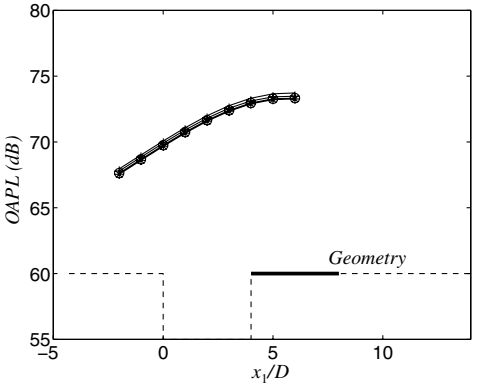

b) Integration from the trailing edge and 4*D* downstream

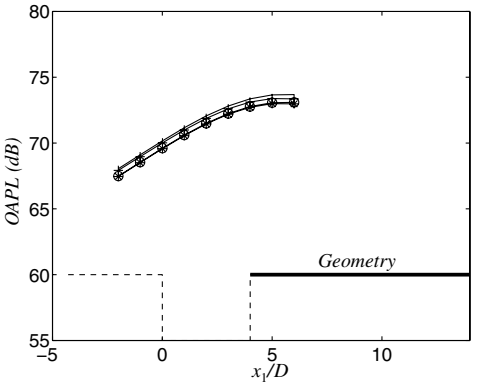

c) Integration from the trailing edge and 10*D* downstream

Fig. 11 OAPL when successively increasing the integration surfaces: reference (−), C1 (+), C3 (★), and C5 (○).

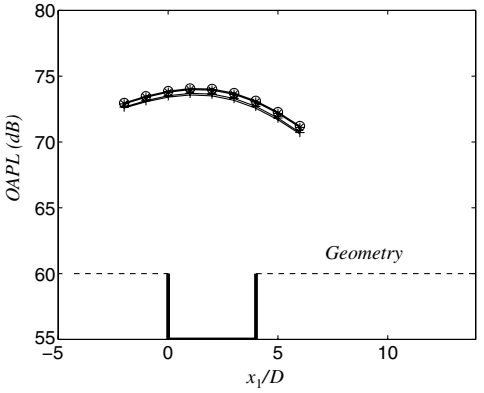

a) Cavity walls

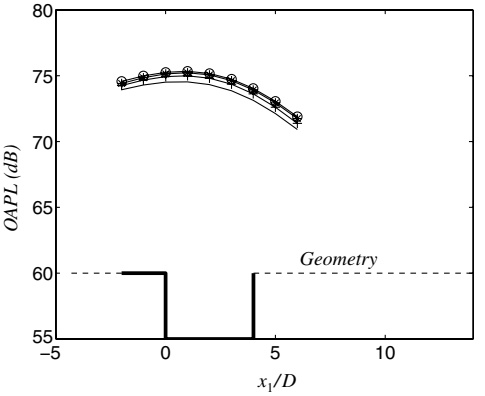

b) Cavity walls and 2*D* upstream

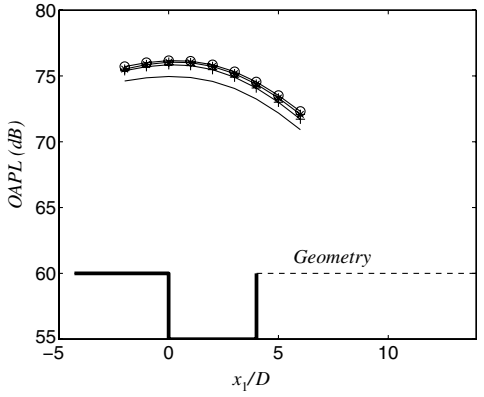

c) Cavity walls and inlet wall

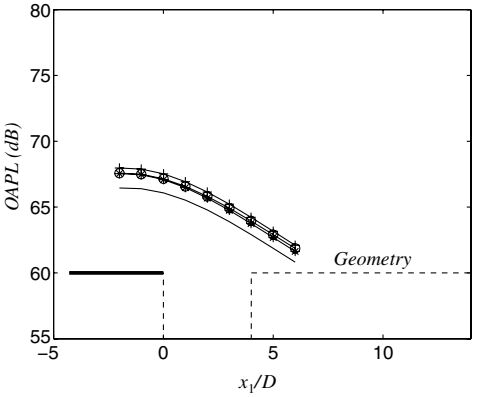

d) Inlet wall

Fig. 12 OAPL at observers when successively increasing the integration surface: reference (−), C1 (+), C3 (★), and C5 (○).

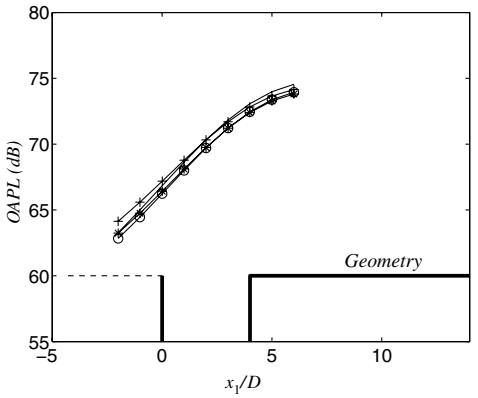

a) Cavity upstream wall, cavity downstream wall, and the outlet wall

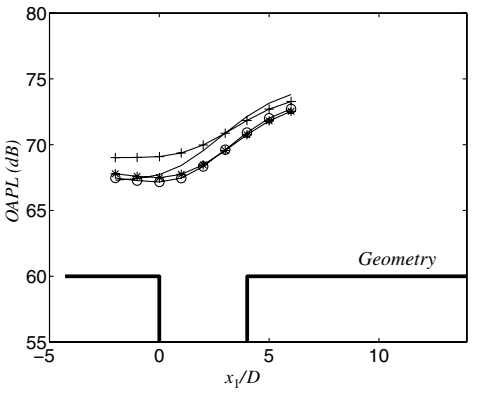

b) Inlet wall, cavity upstream wall, cavity downstream wall, and the outlet wall

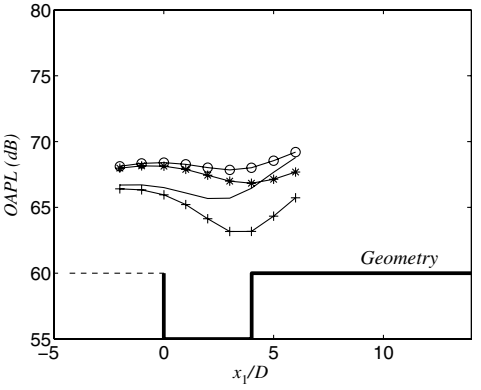

c) Cavity walls and the outlet wall

Fig. 13 OAPL at observers for restricted integration surfaces: reference (−), C1 (+), C3 (⋆), C5 (○).

Fig. 14. The integration region used in this figure contains the walls extending from the inlet to $14D$ downstream of the cavity leading edge, and both source terms are used to obtain the acoustic signals.

For both cases, C1 and C5, recall that the computational time step is $\Delta t = 0.005D/U_\infty$. The effect of the two major vortices leaving the domain is clearly seen in Fig. 14 as two peaks at time $tU_\infty/D \approx 38$ and $tU_\infty/D \approx 47.5$. With the use of the buffer zone, these disturbances are significantly reduced but seem to amplify the high-frequency oscillations in the time span $35 < tU_\infty/D < 40$. This may be an effect of the buffer zone itself or possibly an effect still present in case C5 but masked due to the distorted pressure field caused by the outlet boundary condition. Because the largest discrepancy was found for observer 7, another possibility is that the oscillations could also be caused by the singularity at the cavity trailing edge, which might create problems for an incompressible flowfield. In addition to the high-frequency oscillation existing in case C1, major discrepancies in the acoustic signals still exist over more or less the whole period. One way to study these possibilities is to plot their individual contribution and their added effect in the same time frame. These results are shown in Fig. 15.

Figure 15 gives the acoustic signals using both source terms for three different sets of surface segments, in which region I contains the walls extending from the cavity leading edge to $14D$ downstream of this point (except the cavity bottom), region II contains the cavity bottom wall, and the total is the contribution for the whole region extending from the cavity leading edge to $14D$ downstream of this point. Figure 15 clearly shows that the total contribution is an effect

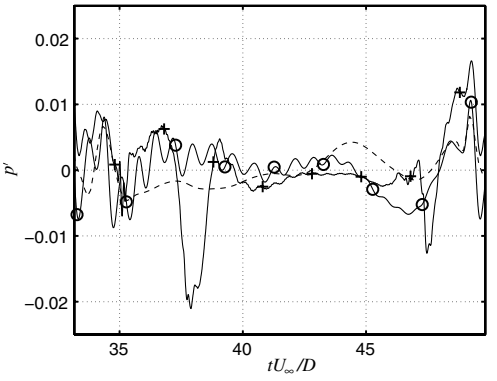

Fig. 14 Acoustic pressure extracted from the last period (see Fig. 6) at observer 7 using both dipole terms for the reference (dashed line), C1 (○), and C5 (+).

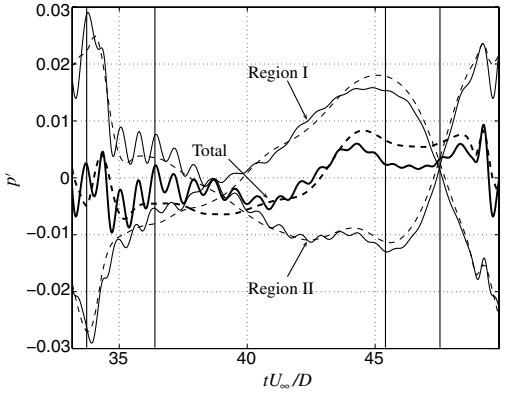

Fig. 15 Acoustic signals at observer 7 using both source terms, region I (cavity leading edge to outlet except cavity bottom), region II (cavity bottom), and total (cavity leading edge to outlet) for reference (dashed lines) and C1 (solid lines).

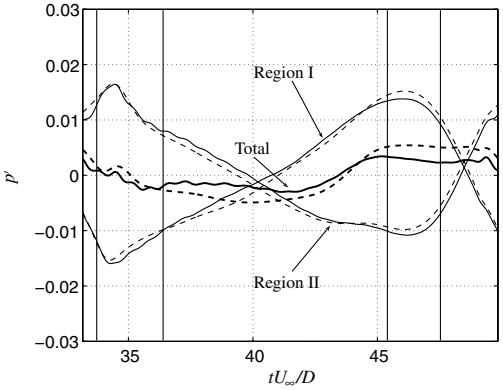

Fig. 16 Acoustic signals at observer 7 using source term one, region I (cavity leading edge to outlet except cavity bottom), region II (cavity bottom), total (cavity leading edge to outlet) for reference (dashed lines) and C1 (solid lines).

of an almost complete cancellation of the sources at region I and region II. Both regions (I and II) show oscillations for the incompressible case. These oscillation are resolved by about 200–300 samples or time steps and are small compared with the peak levels when treated individually. However, when combined (total), the total pressure signal caused by the oscillations is almost as large as the resulting peak level. In fact, the amplitude of the oscillations increases when the two surface regions are brought together, because their phases match. Four vertical lines are also drawn in Fig. 15, representing instants in time when significant differences are found between the compressible and incompressible solutions. At the first instant ($tU_\infty/D \approx 34$), a major mismatch occurs, primarily due to an overprediction of the acoustic pressure at the cavity bottom wall for the incompressible case. At the second instant ($tU_\infty/D \approx 36.5$), the incompressible signal is overpredicted, primarily because of a phase match of the oscillation, but the level of the acoustic pressure is also overpredicted for both segments in the incompressible case. At the third instance ($tU_\infty/D \approx 45.5$), the oscillations are small, but the acoustic pressures for both surface segments are underpredicted in the incompressible case. At the final instance ($tU_\infty/D \approx 47$), the underpredicted acoustic pressure found for the incompressible case causes a major error in the acoustic pressure.

To check if one of the two source terms is possibly more prone to give the discrepancies in the acoustic signals, their contributions are plotted separately. Figure 16 shows the contributions from the first source term (i.e., the surface pressure term). The integration regions and observer are the same as in Fig. 15.

No major differences are present at the first two instants in time ($tU_\infty/D \approx 34$ and $tU_\infty/D \approx 36.5$) in Fig. 16, and the errors detected in Fig. 15 are therefore caused by the second source term. Major differences occur between instants 3 and 4, however, and the offset is therefore primarily related to the first source term. At instant 3 the result in Fig. 16 points toward a combination of errors caused by both source terms if a comparison is made with Fig. 15.

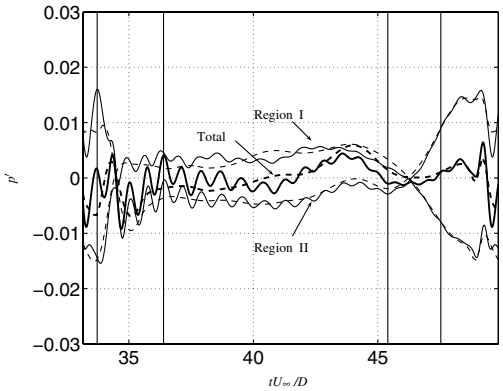

Fig. 17 Wall segment contribution at observer 7, source term 2.

Instant 4 is, for the first source term, not located at the intersection between region I and region II signals; as Fig. 15 shows, the rapid change in signals is therefore amplified by source term 2. In the final figure (Fig. 17), the corresponding results are shown for source term 2.

Figure 17 supports the argument that the oscillations are due to the second source term. Errors in source term 1 were shown in Fig. 16 to be related to the intermediate and last part of the sequence. In contrast, the errors in source term 2 are instead related to the first part of the sequence. One cause of the results in the range $35 < tU_\infty/D < 40$ is synchronous oscillations that are amplified when brought together. One interesting finding is that the oscillations are more pronounced for the cavity bottom wall (region II) as compared with region I. The oscillations are therefore more probably caused by the cavity trailing edge. Further, at instant 1, the difference detected in Fig. 15 occurs, owing to a peak in source term 2.

What then is the physical interpretation of the acoustic signals presented? After $tU_\infty/D \approx 34.5$ the flow starts to make a sharp, almost 90 deg, directional change at the cavity trailing edge. Correspondingly, at $tU_\infty/D \approx 34$ the oscillations in the incompressible case (Fig. 17) are also found to be the highest. A compressible fluid can compensate for this by expanding, whereas an incompressible fluid can only balance between flow speed and pressure, and it is therefore most probable that the oscillations are caused by the singularity at the trailing edge. Studying Figs. 7c–7h, the change in the direction of the flow at the cavity trailing edge gradually becomes smaller and eventually vanishes. This corresponds well to the amplitude of the oscillations (Fig. 17), which also gradually decays.

VI. Conclusions

Incompressibility is a common assumption for low-Mach-number hydrodynamic-dominated flows and has recently also been used quite frequently in combination with acoustic analogies to predict the radiated sound. However, this aspect has not been well investigated and deserves additional attention, which is highlighted in this work.

The case investigated is the laminar flow past an open $2D$ cavity. The given flow conditions result in a wake-mode oscillatory flowfield with large variation in the streamwise force coefficient. Here, incompressible simulations are compared with a direct simulation at Mach number 0.15. An attractive aspect of the present case is that the flow is hydrodynamically dominated. The present Mach number is also sufficiently low for the incompressible assumption to apply. The radiated sound is then computed through Curle's analogy written in temporal form and is evaluated at nine discrete observers located $7.18D$ above the cavity. The noise directivity is evaluated by comparing two dipole terms containing the fluctuating wall pressure and its temporal derivative for the two flowfields. These two terms were identified in previous studies of the same case as the dominating terms and are the only terms treated in the acoustic analogy.

The results regarding the flow properties agree well between the different flowfields in both periodicity and streamwise force contribution. The mean drag for the incompressible cases varies between $0.377 < \bar{C}_D < 0.379$ and corresponds well with the reported compressible results, which vary from $\bar{C}_D = 0.377$ to 0.384, and the Strouhal number for the incompressible cases was $St_L = 0.245$, compared with the reported compressible results that vary between $0.243 < St_L < 0.245$.

With regard to the two investigated acoustic sources, good agreement was found between the different flowfields, especially for the fluctuating-wall-pressure term. The second term shows generally good agreement, with minor discrepancies close to the inlet and outlet. The discrepancy at the inlet is believed to be caused by the different treatments at the inlet in the reference case and the incompressible cases. It is also seen that the buffer zone primarily affects the pressure temporal derivative term but has no significant effect on the level of the fluctuating pressure term.

This analysis gives strong indications that the trailing edge together with the incompressible treatment of the flow are the most

probable causes of the present results, which cause oscillations in the pressure temporal derivative term as well as differences in the surface pressure term due to a different flow behavior. Because the noise emissions are mainly due to more or less complete cancellations of different sources, their representation is vital to obtaining acceptable results. It is therefore strongly recommended that a compressible description of the flow is used when considering noise radiation, at least for cases with rapid geometrical changes and few but strong flow structures.

Acknowledgments

This work was supported by Volvo Car Corporation and the Swedish Agency for Innovation Systems (VINNOVA). I also would like to thank Johan Larsson, who kindly let me use his database for the validation case.

References

[1] Gharib, M., and Roshko, A., "The Effect of Flow Oscillations on Cavity Drag," *Journal of Fluid Mechanics*, Vol. 177, 1987, pp. 501–530. doi:10.1017/S002211208700106X

[2] Colonius, T., Basu, J., and Rowley, C., "Computation of Sound Generation and Flow/Acoustic Instabilities in the Flow Past an Open-Cavity," 3rd ASME/JSME Joint Fluids Engineering Conference, American society of Mechanical Engineers, Fluids Engineering Div., Paper 99-7228, 1999.

[3] Shieh, M., and Morris, P., "Parallel Computational Aeroacoustic Simulation of Turbulent Subsonic Cavity Flow," AIAA/CEAS Aeroacoustics Conference and Exhibit, AIAA Paper 2000-1914, 2000.

[4] Rowley, C. W., Colonius, T., and Basu, A. J., "On Self-Sustained Oscillations in Two-Dimensional Compressible Flow over Rectangular Cavities," *Journal of Fluid Mechanics*, Vol. 455, 2002, pp. 315–346.

[5] Larsson, J., "Computational Aero Acoustics for Vehicle Applications," Licentiate Thesis, Chalmers Univ. of Technology, Göteborg, Sweden, 2002.

[6] Larsson, J., Davidson, L., Olsson, M., and Eriksson, L., "Aero Acoustic Investigation of an Open-Cavity at Low Mach Number," *AIAA Journal*, Vol. 42, No. 12, 2004, pp. 2462–2473. doi:10.2514/1.1339

[7] Colonius, T., "An Overview of Simulation, Modeling and Active Control of Flow/Acoustic Resonance in Open Cavities," AIAA/CEAS Aeroacoustics Conference and Exhibit, AIAA Paper 2001-0076, 2001.

[8] Ask, J., and Davidson, L., "An Acoustic Analogy Applied to the Laminar Upstream Flow over an Open 2D Cavity," *Comptes Rendus. Mécanique*, Vol. 333, No. 9, 2005, pp. 660–665. doi:10.1016/j.crme.2005.07.005

[9] Ffowcs Williams, J. E., and Hawkings, D. L., "Sound Generation by Turbulence and Surfaces in Arbitrary Motion," *Philosophical Transactions of the Royal Society of London, Series A: Mathematical and Physical Sciences*, Vol. 264, No. 1151, 1969, pp. 321–342. doi:10.1098/rsta.1969.0031

[10] Curle, N., "The Influence of Solid Boundaries upon Aerodynamic Sound," *Proceedings of the Royal Society of London A*, Vol. 231, 1955, pp. 505–514. doi:10.1098/rspa.1955.0191

[11] Rung, T., Eschricht, D., Yan, J., and Thiele, F., "Sound Radiation of the Vortex Flow past a Generic Side Mirror," 8th AIAA/CEAS Aeroacoustics Conference, Breckenridge, CO, AIAA Paper 2002-2340, 17–19 June 2002.

[12] Pérot, F., Auger, J., and Giardi, H., "Numerical Prediction of the Noise Radiated by a Cylinder," 9th AIAA/CEAS Aeroacoustics Conference, Hilton Head, SC, AIAA Paper 2003-3240, 12–14 May 2003.

[13] Posson, H., and Pérot, F., "Far-Field Evaluation of the Noise Radiated by a Side Mirror Using LES and Acoustic Analogy," 12th AIAA/CEAS Aeroacoustics Conference, Cambridge, MA, AIAA Paper 2006-2719, 8–10 May 2006.

[14] Ask, J., "A Study of Incompressible Flow Fields for Computational Aero Acoustics," Licentiate Thesis, Chalmers Univ. of Technology, Göteborg, Sweden, 2005.

[15] Davidson, L., and Farhanieh, B., "CALC-BFC, A Finite-Volume Code Employing Collocated Variable Arrangement and Cartesian Velocity Components for Computation of Fluid Flow and Heat Transfer in Complex Three-Dimensional Geometries," Chalmers Univ. of Technology, Dept. of Thermo and Fluid Dynamics, Göteborg, Sweden, 1995.

[16] Tam, C., and Webb, J., "Dispersion-Relation-Preserving Finite Difference Schemes for Computational Acoustics," *Journal of Computational Physics*, Vol. 107, No. 2, 1993, pp. 262–281. doi:10.1006/jcph.1993.1142

[17] Leer, V., "Towards the Ultimate Conservative Difference Scheme II. Monotonicity and Conservation Combined in a Second-Order Scheme," *Journal of Computational Physics*, Vol. 14, No. 4, 1974, pp. 361–370. doi:10.1016/0021-9991(74)90019-9

C. Bailly
Associate Editor